






Article

Structural and Electrical Investigation of Cobalt-Doped NiO_x/Perovskite Interface for Efficient Inverted Solar Cells

Zahra Rezay Marand ^{1,2}, Ahmad Kermanpur ², Fathallah Karimzadeh ², Eva M. Barea ¹, Ehsan Hassanabadi ^{1,3}, Elham Halvani Anaraki ², Beatriz Julián-López ¹, Sofia Masi ^{1,*} and Iván Mora-Seró ^{1,*}

¹ Institute of Advanced Materials (INAM), Universitat Jaume I, Av. Sos Baynat, s/n, 12071 Castelló, Spain; z.rezay@ma.iut.ac.ir (Z.R.M.); barea@uji.es (E.M.B.); hassanab@uji.es (E.H.); julian@uji.es (B.J.-L.)

² Department of Materials Engineering, Isfahan University of Technology, Isfahan 84156-83111, Iran; ahmad_k@cc.iut.ac.ir (A.K.); karimzadeh_f@cc.iut.ac.ir (F.K.); elhamhalvani@gmail.com (E.H.A.)

³ Textile Engineering Department, Textile Excellence & Research Centers, Amirkabir University of Technology, Tehran 15916-34311, Iran

* Correspondence: masi@uji.es (S.M.); sero@uji.es (I.M.-S.)

Received: 24 March 2020; Accepted: 15 April 2020; Published: 30 April 2020



Abstract: Inorganic hole-transporting materials (HTMs) for stable and cheap inverted perovskite-based solar cells are highly desired. In this context, NiO_x, with low synthesis temperature, has been employed. However, the low conductivity and the large number of defects limit the boost of the efficiency. An approach to improve the conductivity is metal doping. In this work, we have synthesized cobalt-doped NiO_x nanoparticles containing 0.75, 1, 1.25, 2.5, and 5 mol% cobalt (Co) ions to be used for the inverted planar perovskite solar cells. The best efficiency of the devices utilizing the low temperature-deposited Co-doped NiO_x HTM obtained a champion photoconversion efficiency of 16.42%, with 0.75 mol% of doping. Interestingly, we demonstrated that the improvement is not from an increase of the conductivity of the NiO_x film, but due to the improvement of the perovskite layer morphology. We observe that the Co-doping raises the interfacial recombination of the device but more importantly improves the perovskite morphology, enlarging grain size and reducing the density of bulk defects and the bulk recombination. In the case of 0.75 mol% of doping, the beneficial effects do not just compensate for the deleterious one but increase performance further. Therefore, 0.75 mol% Co doping results in a significant improvement in the performance of NiO_x-based inverted planar perovskite solar cells, and represents a good compromise to synthesize, and deposit, the inorganic material at low temperature, without losing the performance, due to the strong impact on the structural properties of the perovskite. This work highlights the importance of the interface from two different points of view, electrical and structural, recognizing the role of a low doping Co concentration, as a key to improve the inverted perovskite-based solar cells' performance.

Keywords: inverted planar perovskite solar cell; hole transport material; Co-doped NiO_x; perovskite morphology; electrical conductivity

1. Introduction

Organic-inorganic halide perovskite solar cells (PSCs) have gained increasing attention owing to their high power conversion efficiencies and fabrication in solution at low temperatures. Within just a few years, PSCs have boosted efficiency to 25.2% [1]. Moreover, low-temperature processing makes them promising for future industrialization [2]. Along with the improvement in the perovskite material and deposition techniques, the advances in perovskite solar cells are also due to the study of the different

hole-transporting and electron-transporting materials (HTMs and ETMs, respectively) employed in the devices [3]. The two most common architecture used in the fabrication of PSCs are the *n-i-p* and *p-i-n* configurations and the current highest efficiencies are achieved with the *n-i-p* one, using TiO₂ as ETM and doped Spiro-OMeTAD as HTM [4]. This configuration is characterized by the high cost of the HTM and by a slight hysteresis, which has to be avoided with the use of special treatment or interlayers [5]. This hysteretic behavior can also be suppressed by using inverted *p-i-n* architectures [6–8]. Moreover, the planar *p-i-n* configuration is more favorable due to its relatively low-temperature processing, primarily when organic HTM is used [9,10]. However, one of the challenges in the fabrication of inverted perovskite solar cells is the lack of stable and low-cost HTM: i.e., poly(3,4-ethylenedioxythiophene):poly(styrenesulfonate) (PEDOT:PSS) has high acidity, which decreases the long-term stability of the devices [11], and the poly[*N,N'*-bis(4-butylphenyl)-*N,N'*-bisphenylbenzidine] (p-TPD) and the poly(triaryl amine) (PTAA) are expensive and very hydrophobic, hindering the easy perovskite deposition, due to the poor wettability [12]. Conversely, inorganic materials like, MoO_x, CuCrO₂, CuO_x, CuSbS₂, CuSCN and NiO_x, have low-cost and superior stability as well as higher mobility, basic prerequisites for obtaining stable and high-efficiency perovskite solar cells.

Among the inorganic HTMs, the low-temperature NiO_x is the most common in PSCs [13–16]. The remarkable properties of NiO_x, such as intrinsic p-type doping nature, high optical transmittance, deep-lying valence band (VB) (5.4 eV) and low cost, make NiO_x a preferential candidate for HTM in PSCs. NiO_x has been prepared by several methods such as spray pyrolysis and a solution process or pulsed laser deposition [14,17–19]. Despite the merits of NiO_x as HTM, its low intrinsic electrical conductivity and the high amount of defects when it is synthesized at low temperature, resulting in an increased charge recombination and reduced hole extraction [20], have blocked further improvement to NiO_x-based PSCs. To overcome this drawback, keeping the temperature low, two main methods have been investigated, one is the addition of interlayers to control the interface [21] and a more effective one is metal ion doping. Different metals are used to dope the NiO_x, like Au⁺ [13], Cu²⁺ [22], Co³⁺ [23] and Li⁺ [24]. Among different metals, Co is a promising dopant, yet used for other materials in direct solar cells configuration [25–27]. With regard to the NiO_x, due to the low lattice parameter mismatch of 1.6% [28], a power conversion efficiency (PCE) of 18% has been obtained [29], but with an annealing around 300–400 °C [30]. Low-temperature synthesis of Co-doped NiO_x has been further optimized, and an improvement of the conductivity when the level of doping increases has been demonstrated [17]. However, the maximum efficiency is obtained at a doping level (1%) lower than that needed to obtain the maximum conductivity (5%), because a decrease of the hole extraction ability [17]. Here we have developed the low temperature synthesis of Co-doped NiO_x nanoparticles with Co ion from 0.75 to 5 mol% to stay in the range of higher conductivity and good hole extraction properties [23]. A comparative analysis of the structural and optical properties of the perovskite material, when deposited on the inorganic HTM, is also carried out. Although the conductivity is almost the same in the case of the NiO_x doped and not doped by Co, we demonstrated that the Co doping leads to an increase of perovskite layer morphology and a change in the recombination mechanism. This is correlated with the increased fill factor (FF) in the solar cells—usually low due to the high temperature deposition (Table 1) employed and for the generation of defects in the bare NiO_x devices—in turn due to the increased perovskite crystallinity and to the morphological improvement when the Co doping is employed as high as 0.75 mol%, assisting in the reduction of the more hostile bulk recombination [31–33].

Table 1. NiO_x processing temperature and the corresponding best efficiency obtained for inverted perovskite solar cells; ITO: Indium tin oxide; PCBM: Phenyl-C61-butyric acid methyl ester; BCP: bathocuproine.

Device Configuration	NiO _x Processing Temperature	Increasing FF (%) by Adding Dopant	PCE (%)	Refs.
Glass/ITO/Co-NiO _x /CH ₃ NH ₃ PbI ₃ /PCBM/BCP/Ag	130 °C	6	16.42	This work
Glass/ITO/Co-NiO _x /CH ₃ NH ₃ PbI ₃ /PCBM/BCP/Ag	130 °C	6	14.5	[23]
Glass/ITO/Co-NiO _x /CH ₃ NH ₃ PbI ₃ /PCBM/PEI/Ag	400 °C	2	18.5	[29]
Glass/FTO/NIR-Co-NiO _x /CH ₃ NH ₃ PbI ₃ /PCBM/PEI/Ag	300 °C	0	17.77	[30]
Glass/ITO/Co-NiO _x (solution-processed)/CH ₃ NH ₃ PbI ₃ /PCBM/C60/Ag	340 °C	10	17.52	[34]

2. Experimental Section

2.1. Materials

Ni(NO₃)₂·6H₂O (99.9%) and CoCl₂·6H₂O (99.0%), were purchased from Sigma Aldrich (Madrid, Spain). Lead iodide (PbI₂, >98%, from TCI, Tokyo, Japan), methylammonium iodide (MAI, 98%, from Greatcellsolar, Queanbeyan, Australia), 2-propanol (99.7% from Carlo Erba, Val de Reuil, France), ethanol (96%) and acetone (99.25%) from PanReac (Castellar del Valles, Spain), hydrochloric acid (HCl 37%), dimethyl sulfoxide (DMSO anhydrous 99.9%), chlorobenzene (CB anhydrous 99.8%), ethylacetate (EA anhydrous 99.8%), zinc powder (99.995%) from Sigma aldrich. [6,6]-Phenyl-C61-butyric acid methyl ester (PCBM, 99%) was purchased from nano-C (Westwood, NJ, USA). 2,9-Dimethyl-4,7-diphenyl-1,10-phenanthroline (BCP, 99%) was purchased from Sigma Aldrich.

2.2. Synthesis of NiO_x and Co-Doped NiO_x Nanoparticles

The NiO_x was synthesized following previous reports [23]. The different steps of the synthesis are summarized in Figure 1. NiO_x nanoparticles doped with different amounts of Co with different molar ratios ($x = 0, 0.75, 1, 1.25, 2.5$ and 5 mol%) were synthesized using the chemical co-precipitation method, according to the method reported in literature [35]. The typical procedure is as follows: Ni(NO₃)₂·6H₂O (0.25 mol) was dissolved in 50 mL of deionized deoxygenated H₂O to obtain a dark green solution. After being vigorously magnetically stirred for 1 h, NaOH solution (10 M, alkali source) in drops was added to the initial solution by slower stirring for crystallizing structures. During this operation, the initial dark green color of the solution turned to opaque pale green as a result of nanoparticles formation. Then keeping it stirred for another 1 h, the pale green colloidal precipitate was collected by an ultrasonic centrifugation at 6500 rpm for 15 min, and washed twice with deionized water. Finally, the product was dried at 80 °C overnight. The green solid obtained was grinded in mortar then calcined at 270 °C for 2 h to obtain a black powder. It is worth mentioning that all main synthesis steps were performed under N₂ gas protection to create an oxygen-free atmosphere and prevent oxidation of divalent nickel salts. For doping, divalent Co (Co²⁺), CoCl₂·6H₂O was added to the Ni(NO₃)₂·6H₂O solution at various molar ratios which were mentioned above. Before use, nanoparticles were dispersed in deionized water by ultrasonics probe for 2 min with amplitudes of 52% and cycle 1 (20 mg mL⁻¹). Finally, the nanoparticle solution was filtered through a PVDF filter (0.40 μm).

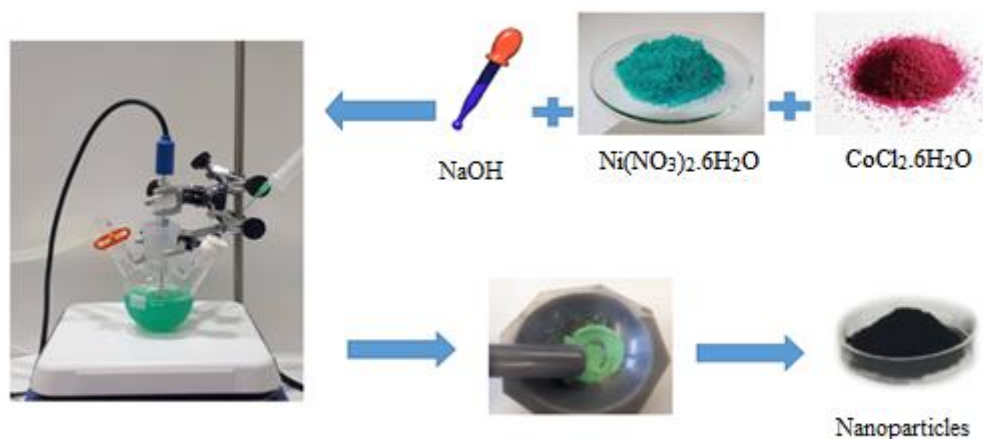


Figure 1. Sketch of the Co-doped NiO_x nanoparticles synthesis.

2.3. Fabrication of Solar Cells

Substrates (tin-doped indium oxide-ITO) were etched with zinc powder and HCl 6 M. After cleaning with soap and water and then placing in an ultrasonic bath with 2% Extran solution in water for 15 min with ethanol, isopropanol, and acetone for 15 min for each solvent, the substrate were dried by airflow and were put in an ultraviolet–ozone (UV-O₃) environment for 10 min to remove organic residues. The HTMs were obtained by spin-coating the corresponding NiO_x or Co-NiO_x aqueous solution (20 mg mL⁻¹) with a speed of 3000 rpm for 40 s and heated at 130 °C for 10 min, in ambient conditions. The perovskite film (MAPbI₃) was deposited over the HTM layer by one-step spin coating at 2000 rpm for 10 s, followed by 6000 rpm for 28 s with an acceleration of 3000, with the precursor composed of PbI₂ and MAI (1.3 M for each) in 1 mL DMSO. Ethyl acetate was dropped onto the perovskite film at the last 15th second during the spin coating. As soon as the spin coating was finished, the sample was moved to a hotplate and annealed for 10 min at a temperature 130 °C [36]. Afterward, PCBM (20 mg mL⁻¹ in CB) was spin-coated at 1000 rpm for 30 s and dried at 60 °C for 10 min. BCP (0.5 mg mL⁻¹ in 2-propanol) was deposited by spin-coating at 6000 rpm for 30 s and dried at 60 °C for 5 min. Finally, Ag electrodes with a thickness of 100 nm were thermally evaporated at a deposition rate of about 0.5 nm s⁻¹ in a vacuum chamber through a shadow mask [37].

2.4. Structural Characterization

The morphologies of the samples (ITO/Co-NiO_x/MAPbI₃) were characterized with a field-emission scanning electron microscope (FEG-SEM JEOL 3100F) operated at 5 kV, equipped with energy-dispersive X-ray spectroscopy. The X-ray diffraction (XRD) patterns of the NiO_x and Co-NiO_x powders were recorded using an X-ray diffractometer (D8 Advance, Bruker AXS, Karlsruhe, Germany) (Cu K α , the wavelength of $\lambda = 1.5406 \text{ \AA}$) within the range of 30–70°. Transmission electron microscopy (TEM) images were recorded using (JEOL 2100 microscope, Akishima, Japan). Surface morphologies of thin films were observed using an atomic force microscope (AFM) (CSI-Nano Observer, Les Ulis, France).

2.5. Optoelectronic Characterization

The current–voltage (*J/V*) curves were measured using a Keithley 2612 source meter under AM 1.5 G (100 mWcm⁻²) provided by a solar simulator model 69,920 Newport. Each curve was generated using 123 data points. The active area of the cell is 0.121 cm², and the scan rate was 10 mVs⁻¹. The incident photons to current efficiency (IPCE) measurements were performed with a QEPVSI-b Oriel measurement system. The steady-state absorption spectra of the perovskite films were achieved by using an ultraviolet–visible (UV/Vis) absorption spectrophotometer (Varian, Cary 300, Palo Alto, CA, USA), and the steady state and the time-resolved photoluminescence (PL) decay were collected by

a Horiba Fluorolog. The steady state PL was collected at a wavelength of 780 nm after excitation at 532 nm.

3. Results and Discussion

To investigate in detail how the presence of very low content of Co dopant (0.75–5 mol%) in the nickel oxide structure influencing the properties of the PSCs, a first characterization of NiO_x nanoparticles was made. TEM images of NiO_x nanoparticles and NiO_x with different Co percentage as dopant are shown in Figure 2. Pure NiO_x nanoparticles have a broad size distribution (10–33 nm) centered at 17 nm. However, the Co-doped particles present a smaller average size around 12 nm, and a narrower size distribution than the undoped nanoparticles. These results are in good agreement with the crystal size calculated from the XRD measurements (Figure 3a) using the Debye–Scherrer formula, see Table S1 [38,39].

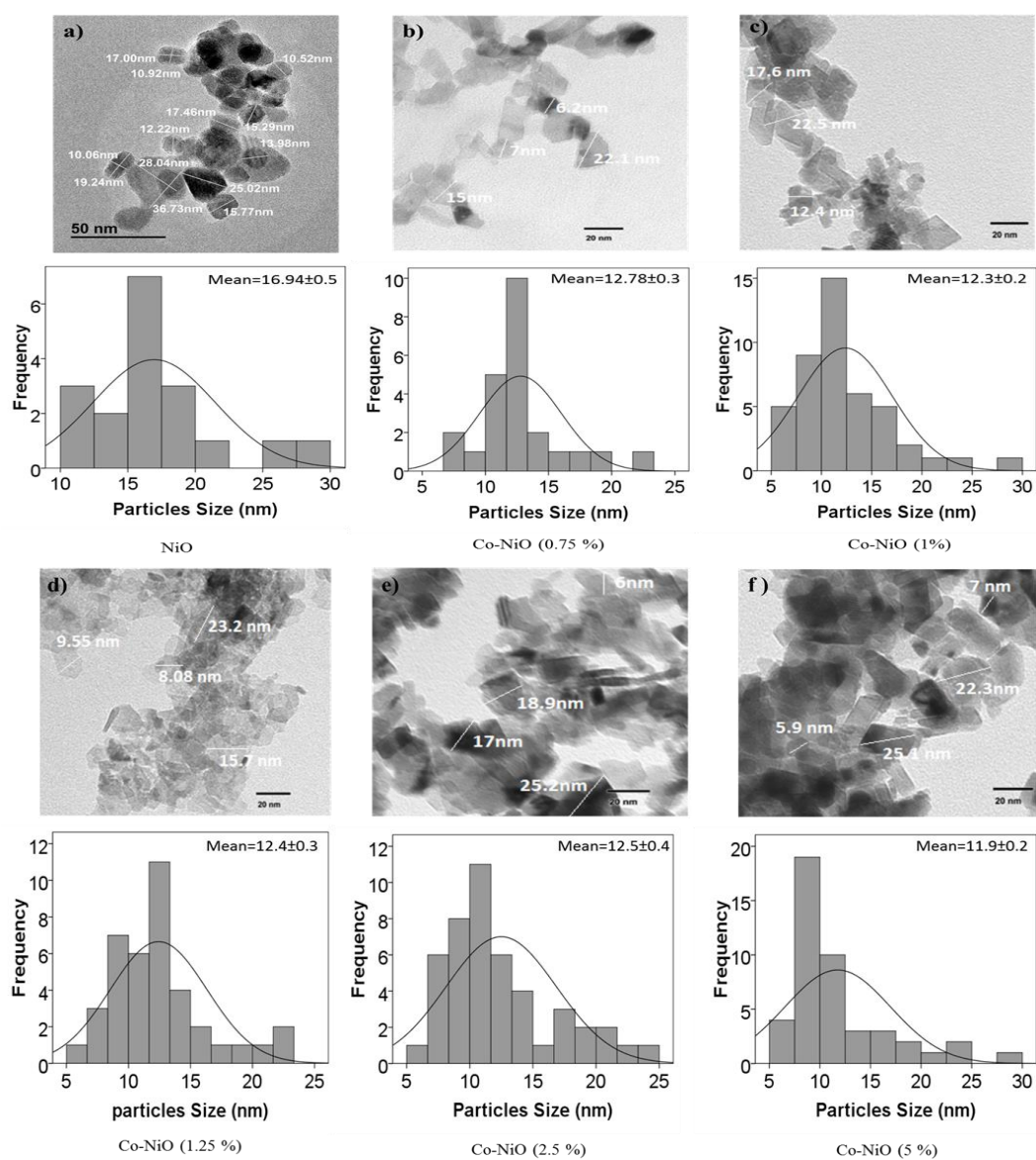


Figure 2. Transmission electron microscopy (TEM) images and relative histograms of the nanoparticles size distributions of (a) NiO_x nanoparticles; (b) 0.75 mol% Co-NiO_x nanoparticles; (c) 1 mol% Co-NiO_x nanoparticles; (d) 1.25 mol% Co-NiO_x nanoparticles; (e) 2.5 mol% Co-NiO_x nanoparticles; (f) 5 mol% Co-NiO_x nanoparticles.

XRD peaks of all samples correspond to the standard pattern characteristic of the cubic crystal structure of NiO_x , with three characteristic diffraction peaks at 37.1° , 43.0° and 62.7° related to (111), (200) and (220) planes of NiO_x , respectively (Figure 3a). No secondary phase is detected, ruling out the formation of other Co-based structures such as CoO. Therefore, the NiO_x has been formed with relatively high phase purity and, according to the difference in the peaks intensities between the samples of undoped NiO_x and Co-doped NiO_x , it is clear that Ni ions have been successfully replaced with Co ions, as demonstrated also by energy-dispersive X-ray spectroscopy (EDS) measurements (Figure S1) [40]. We investigated the optical characteristics of the pristine NiO_x and Co- NiO_x films. The Co- NiO_x films deposited on the ITO substrates revealed a high transmission ($>87\%$) in the visible region (400–800 nm) (Figure 3b). [23] Concerning the optical properties of the Co- NiO_x films, they showed a slightly lower transmission than undoped films, see Figure 3b.

NiO_x and Co-doped NiO_x nanoparticles were deposited in thin film in order to work as HTM. The surface morphologies of pure NiO_x and Co- NiO_x films are shown in Figure 4. The Co- NiO_x films consisted of smaller-sized grains than the pure NiO_x film and the 0.75 mol% show the most uniform morphology over a large area [23].

MAPbI_3 films were deposited on top of the NiO_x or Co- NiO_x HTM. The SEM images (Figure 5a–f) indicated similar polycrystalline morphologies, uniform and pinhole-free perovskite with smaller grain sizes (~ 150 – 200 nm) on the top of NiO_x film and the biggest size is for the Co doping percentage 2.5 and 5 mol%). The bigger grain size could be due to better morphology of the Co-doped substrate. Between the different doping percentages, the 0.75 mol% Co- NiO_x film, that present the best morphology, produce also the second for dimension perovskite grains, of ~ 250 – 300 nm (Figure 5b), together with a more uniform distribution (Figure S2). The uniformity of the inorganic HTM and the big grains of the perovskite, demonstrate the potential of the 0.75 mol% doping for the fabrication of high-quality optoelectronic devices. The XRD spectra of perovskite layers (Figure 5g) show the presence of six main peaks at 14.20° , 19.94° , 23.56° , 28.50° , 31.75° , and 40.67° , which correspond to the (110) (112) (202) (220) (310) and (224) planes for the perovskite MAPI_3 [36]. Moreover, the perovskite growth on the NiO_x substrate doped with 0.75 mol% of Co is the more crystalline and oriented one, as the intensity of the peak at 14.20° and the ratio between the (110) and (220) faces are the highest (Table S2). The benefits of growing crystal with large grain size and good orientation are, firstly, the reduced grain boundary area associated with large grains. The reduced grain boundary area suppresses bulk defects, charge trapping and decreases recombination, with the consequence of a relative higher carrier mobility. This is also translated in the device, in which the photo-generated carriers can easily propagate without frequent encounters with defects and impurities [41], see below.

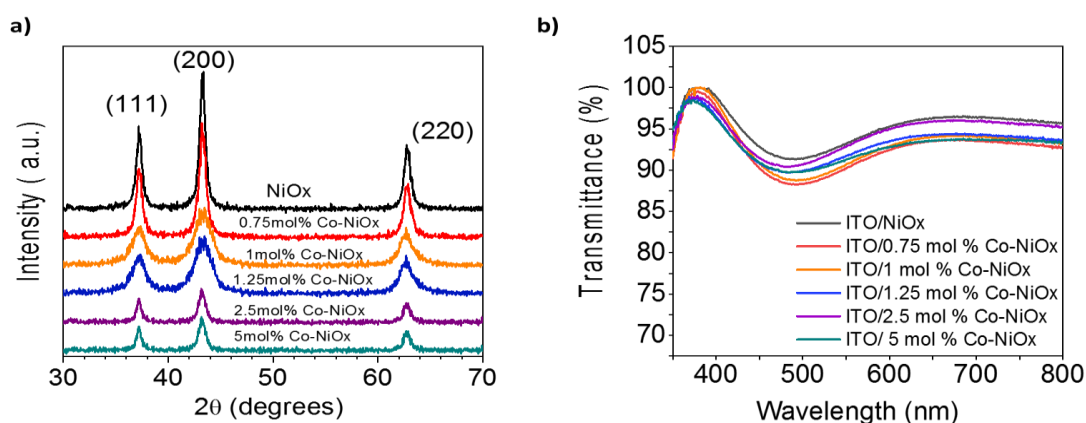


Figure 3. (a) X-ray diffraction (XRD) patterns of the NiO_x and Co-doped NiO_x nanoparticles; (b) optical transmission spectra for the NiO_x and Co- NiO_x films fabricated on top of ITO substrates, where the thickness of the Co- NiO_x films was around 37 nm.

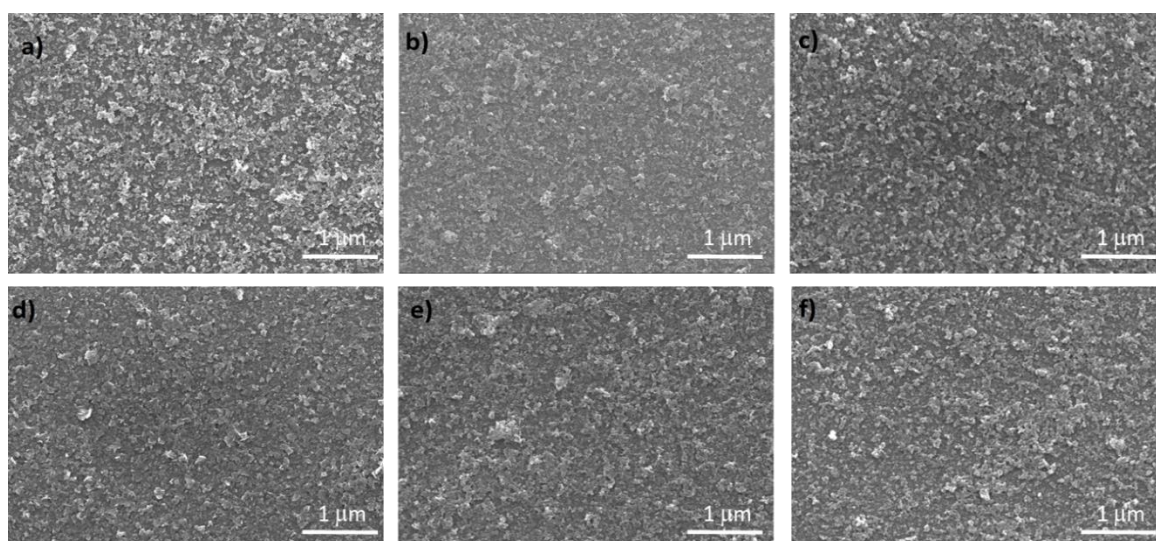


Figure 4. Scanning electron microscopy (SEM) images of the NiO_x and Co-NiO_x films on glass substrate. (a) NiO_x ; (b) 0.75 mol% Co-NiO_x ; (c) 1 mol% Co-NiO_x ; (d) 1.25 mol% Co-NiO_x ; (e) 2.5 mol% Co-NiO_x ; (f) 5 mol% Co-NiO_x .

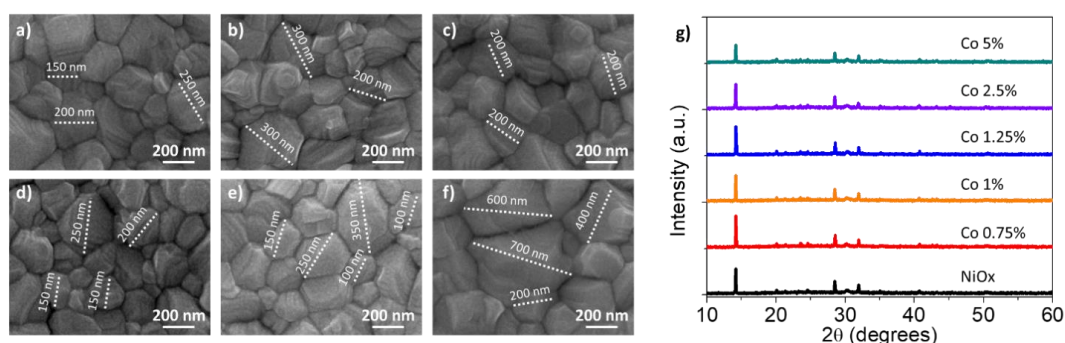


Figure 5. Top view SEM images for perovskite layers fabricated on the top of NiO_x or Co-NiO_x layer; (a) NiO_x ; (b) 0.75 mol% Co-NiO_x ; (c) 1 mol% Co-NiO_x ; (d) 1.25 mol% Co-NiO_x ; (e) 2.5 mol% Co-NiO_x ; (f) 5 mol% Co-NiO_x ; (g) corresponding perovskite X-ray diffraction patterns.

To quantify the effect of Co-NiO_x as HTMs, PSCs have been fabricated and characterized with an inverted structure as shown in Figure 6a (glass/ITO/ NiO_x or Co-NiO_x /MAPbI₃/PCBM/BCP/Ag). The cross section (Figure 6b,c) demonstrates that the thickness of the perovskite is the same (300 nm) on the top of bare NiO_x and Co-NiO_x . It is noted here that better charge transport and low energy loss could be expected for the devices with Co-NiO_x because of the well-matched energy levels to perovskite than the pristine NiO_x [34]. The pristine champion NiO_x -based inverted PSC showed a fill factor (FF) of 70%, a short-circuit current density (J_{sc}) of 19.5 mA cm⁻², a V_{oc} of 0.96 V and a final PCE of 13.2%. By the insertion of the Co ions, J_{sc} , FF and V_{oc} increase, compared with that of pristine NiO_x (Figure 6d) [42,43]. The corresponding device parameters are summarized in Table 2 and the statistics on 40 devices for each type are reported in Figure S3. We achieved a champion PCE of 16.42%, for the 0.75 mol% Co-NiO_x , close to the PCE reported with NiO_x as HTM synthesized at high temperature [29] and the highest reported for low temperature Co-doped NiO_x based inverted perovskite solar cells [23]. The highest FF value was found again for the 0.75 mol% Co-NiO_x device with a value of 76%, compared to 70% for the pristine NiO_x device. Thus, it is clear that a proper Co doping effectively improves the quality of the perovskite materials and enhances the J_{sc} and the general device performance. The stabilized current at maximum power point is also reported in Figure S4. Note that despite 5 mol% Co-NiO_x samples present big grain sizes, see Figure 5f, they also present a

low shut resistance, see Figure 6d, that decreases significantly the FF, see Table 2. This results points to the presence of pinholes probably induced by the fast growth of some grains.

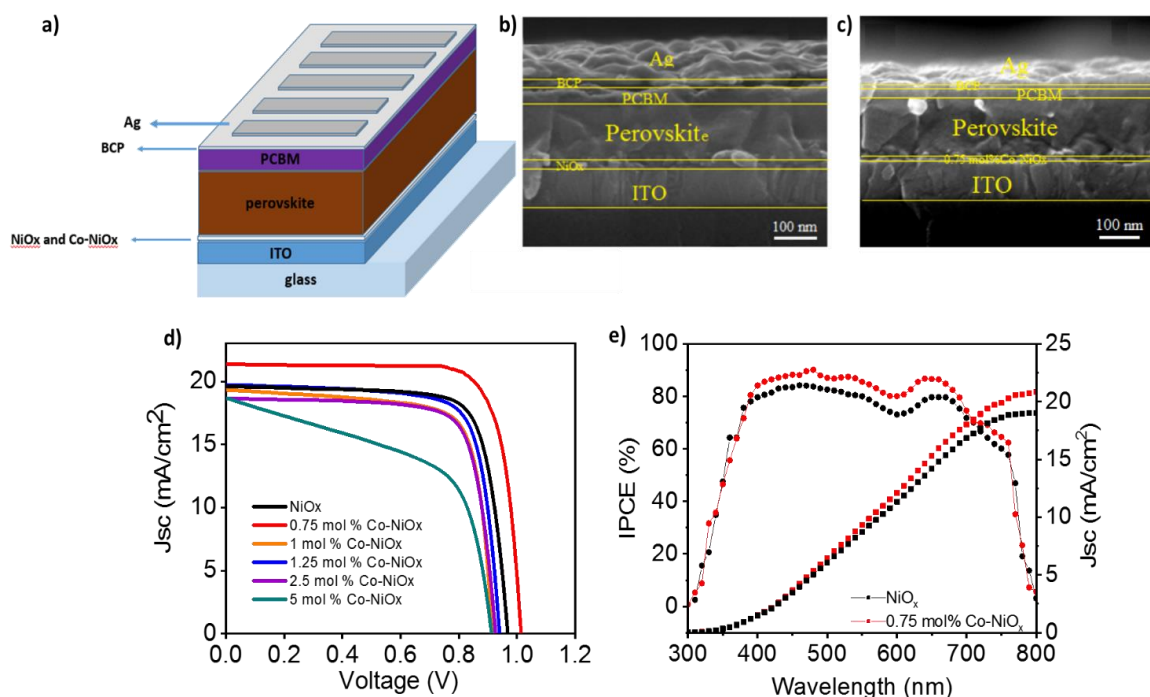


Figure 6. (a) Sketch of the device architecture; Cross-sectional SEM images for perovskite layers fabricated on the top of NiO_x or Co-NiO_x layer: (b) NiO_x and (c) 0.75 mol% Co-NiO_x; (d) *J/V* curves of PSCs using 0.75–5 mol% Co-NiO_x and bare NiO_x as hole-transporter materials (HTMs). (e) incident photons to current efficiency (IPCE) of 0.75 mol% Co-NiO_x and NiO_x based champion base devices.

Table 2. Photovoltaic performance by *J/V* measurements with reverse scan under standard illumination (100 mW cm^{−2}) for champion devices and averaged.

Co-Doping (mol%)	FF (%)	<i>J</i> _{sc} (mA cm ^{−2})	<i>V</i> _{oc} (mV)	Best PCE (%)	Average PCE ± s.d. (%)
0	70	19.5	968	13.2	11.47 ± 1.08
0.75	76	21.5	1005	16.42	14.02 ± 1.3
1	75	19.5	920	13.45	11.66 ± 1.1
1.25	76	19.75	938	14	11.75 ± 1.3
2.5	75	18.7	924	12.9	11.13 ± 0.8
5	56	18.7	910	9.5	8.7 ± 0.6

The IPCE spectra of the champion device shows higher external quantum efficiency for 0.75 mol% Co-NiO_x than the pristine NiO_x device (Figure 6e). The integrated current densities derived from the IPCE spectrum are 21.5 mAcm^{−2} for 0.75 mol% Co-NiO_x and 19.5 mAcm^{−2} for pristine NiO_x, in good agreement with the *J/V* measurements. Moreover, the *J*_{sc} obtained is the highest reported for low-temperature Co-doped NiO_x [23] not caused to the different active layer thickness (Figure 6b,c).

In order to unveil the origin of the better performance of Co-NiO_x samples a systematic optical and electrical characterization was performed. The behavior of the photoluminescence (PL) with NiO_x and Co-NiO_x HTM has been analyzed. Comparing the PL of MAPbI₃ films deposited on glass with the PL of MAPbI₃ deposited on NiO_x and Co-NiO_x films, a significant PL quenching is observed, especially for samples deposited on Co-NiO_x films, see Figure 7a and Figure S5. This fact indicates an increase of the non-radiative recombination at the interface [44]. This point is partially confirmed by the decrease of the PL lifetime measured by time-resolved PL (TRPL), see Figure 7b and Table S3. The perovskite

layer without any HTM showed the average lifetime (τ_{ave}) of photo-generated excitons of 32 ns, while the perovskite layer on pristine NiO_x and Co- NiO_x exhibited τ_{ave} of 20 ns and 9.8 ns (Figure 7b).

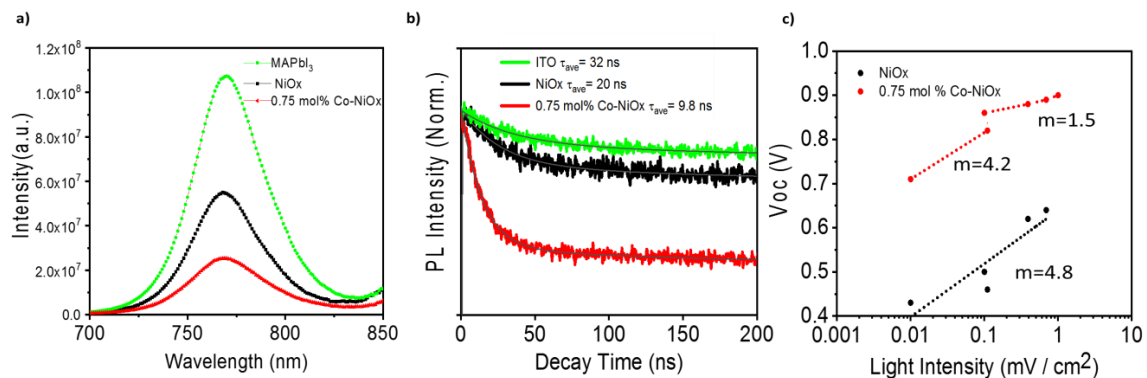


Figure 7. (a) Photoluminescence (PL) of MAPbI₃ films on top of NiO_x and 0.75 mol% Co-NiO_x. The MAPbI₃ on top of glass was used as a reference measurement; (b) time-resolved PL of the corresponding samples; (c) V_{oc} vs. different light intensity for 0.75 mol% Co-NiO_x and NiO_x.

On the other hand, surface roughness and electrical properties of the HTM were analyzed by atomic force microscopy (AFM) and conductive AFM (c-AFM). At this doping level, the improvement of the conductivity is not significant, as we measure by conductive-AFM (Figure S6). The surface roughness of NiO_x and Co-NiO_x films is also the same at about 50 nm, see Figure S6. Since the films roughness was still comparable to the pristine NiO_x film, it confirms again that the Co was effectively embedded in the NiO_x without notable deformation of the rock salt crystal structure [34]. Meanwhile c-AFM measurement shows similar electrical behavior (Figure S6), thus the improvement of performances of PSCs based on Co-NiO_x cannot be attributed to an increase of the electrical conductivity. Therefore, an analysis of the ideality factor, m , of both devices was performed to characterize whether the effect of Co in the structure, in addition to improving the crystallinity and grain size, is to modify the electrical behavior of the device, specifically the electronic recombination.

In order to analyze the recombination, the mechanism m of both samples was obtained from the slope of the V_{oc} dependence with light illumination, see Figure 7c, using the relation: [45,46].

$$e \cdot V_{OC} = E_g + m \cdot k_B \cdot T \cdot \ln \frac{\Phi}{\Phi_0} \quad (1)$$

where e is the electron charge, E_g is the light absorber bandgap, k_B is the Boltzmann constant, T the temperature, Φ is the light intensity and Φ_0 is a constant with the same units than Φ .

For the Co-NiO_x device, two different behaviors are observed, corresponding to high and low light intensity. We determined $m = 4.2$ at low light intensities corresponding to a bulk multiple trapping in trap distribution. However, at high light irradiation m decreases to 1.5, indicating that most of traps are filled at higher light intensity and that the recombination mechanism is now mainly influenced by surface recombination, in good agreement with the PL results. For the NiO_x device (Figure 7c) the recombination mechanism is totally independent from the light intensity, as the device presents the same ideal factor of 4.8, pointing to a higher density of bulk traps, which cannot be filled even at high light intensity.

Taking into account the different characterizations performed on the various devices using NiO_x and Co-NiO_x, focusing concretely on 0.75 mol% that presents the highest performance, we observed two different main trends. On the one hand, an increase of the grain size and improvement of the morphology, which decrease the bulk defects, and on the other hand an increase of the surface recombination. In the case of Co-NiO_x 0.75 mol%, it presents higher and more uniform grain size and we hypothesize that the positive effect of the improvement of the bulk properties compensate for the

deleterious effect of a not-suppressed interfacial recombination, causing a final enhancement of the device performance.

4. Conclusions

In summary, we have investigated the suitability of Co-doped NiO_x nanoparticles as HTMs. Co-NiO_x nanoparticles with a diameter of ~10–20 nm, containing different concentrations (0–5 mol%) of Co ions were synthesized. A comprehensive analysis of optical, morphological and crystallographic investigations demonstrated a double effect of the Co doping. On the one hand, Co doping arises from a surface recombination, on the other hand, Co doping influences the properties of the perovskite grown on top of the Co-NiO_x substrates, improving the morphology as a consequence of a grain size enlargement, and reducing the bulk-recombination. The final performance of the devices prepared with Co-NiO_x as HTM depends on the balance between these two opposite trends. The case of 0.75 mol% Co-NiO_x-based device, that presents a perovskite active layer with big grain size and the highest crystallinity, produces a positive balance and the devices with the highest performance are obtained with champion PCE of 16.42%, higher than previous results with the Co-NiO_x HTM synthesized at low temperature.

Supplementary Materials: The following are available online at <http://www.mdpi.com/2079-4991/10/5/872/s1>, Figure S1: EDS spectra for NiO_x and Co-NiO_x nanoparticles and quantitative analysis for each element (Ni, Co, O). Figure S2: Perovskite grain size statistical distributions of the film deposited on the NiO_x with and without Co doping at different percentage (from 0.75 to 5 mol%). Figure S3: Statistical analysis; Figure S4: Recorded photocurrent at maximum power point J_{MPP} of the champion devices; Figure S5 PL measurement; Figure S6: Conductive-AFM topographies on ITO substrates; Table S1: Grain sizes (nm) of the pure NiO_x and different percentage Co doped nanoparticles, obtained from XRD measurement using the Debye-Scherrer; Table S2: Intensity of the XRD perovskite peaks (counts) and ratio between the intensity of the peaks 110 (14.2°) and 220 (28.5°). Table S3: photoluminescence time decay parameters τ_1 and τ_2 and their average.

Author Contributions: Z.R.M.: Cells Fabrication, Investigation, writing—original draft preparation, A.K.: Resource, Supervision, F.K.: Resource, Supervision, E.M.B.: Data curation, E.H.: Data curation, E.H.A.: Resource, B.J.-L.: Resource, S.M.: Supervision, Data curation, writing—review & editing, I.M.-S.: Supervision, Resource, review & editing. All authors have read and agreed to the published version of the manuscript.

Funding: Z.R.M. acknowledges the Ministry of Science, Research and Technology of Iran for the financial support. We also thank SCIC of University Jaume I for its help with TEM and XRD and SEM measurements. Financial support from the European Research Council (ERC) via Consolidator Grant (724424-No-LIMIT), Universitat Jaume I via DEPE2D UJI-B2019-09 and NENUPHAR UJI-B2018-71, and Generalitat Valenciana via Prometeo Grant Q-Devices (Prometeo/2018/098) are gratefully acknowledged.

Conflicts of Interest: The authors declare no conflict of interest.

References

1. Best Research-Cell Efficiencies. Available online: <https://www.nrel.gov/pv/assets/pdfs/best-research-cell-efficiencies.20200406.pdf> (accessed on 16 April 2020).
2. Deng, Y.; Van Brackle, C.H.; Dai, X.; Zhao, J.; Chen, B.; Huang, J. Tailoring solvent coordination for high-speed, room-temperature blading of perovskite photovoltaic films. *Sci. Adv.* **2019**, *5*, eaax7537. [[CrossRef](#)]
3. Fakharuddin, A.; Schmidt-Mende, L.; Garcia-Belmonte, G.; Jose, R.; Mora-Sero, I. Interfaces in perovskite solar cells. *Adv. Energy Mater.* **2017**, *7*, 1700623. [[CrossRef](#)]
4. Zhu, T.; Su, J.; Labat, F.; Ciofini, I.; Pauporte, T. Interfacial Engineering through Chloride-Functionalized Self-Assembled Monolayer for High-Performance Perovskite Solar Cells. *ACS Appl. Mater. Interfaces* **2020**, *12*, 744–752. [[CrossRef](#)] [[PubMed](#)]
5. Wang, J.; Datta, K.; Weijtens, C.H.L.; Wienk, M.M.; Janssen, R.A.J. Insights into fullerene passivation of SnO₂ electron transport layers in perovskite solar cells. *Adv. Funct. Mater.* **2019**, *29*, 1905883. [[CrossRef](#)]
6. Noh, Y.W.; Lee, J.H.; Jin, I.S.; Park, S.H.; Jung, J.W. Tailored electronic properties of Zr-doped SnO₂ nanoparticles for efficient planar perovskite solar cells with marginal hysteresis. *Nano Energy* **2019**, *65*, 104014. [[CrossRef](#)]
7. Song, J.; Zhang, W.; Wang, D.; Deng, K.; Wu, J.; Lan, Z. Colloidal synthesis of Y-doped SnO₂ nanocrystals for efficient and slight hysteresis planar perovskite solar cells. *Sol. Energy* **2019**, *185*, 508–515. [[CrossRef](#)]

8. Ma, Z.; Zhou, W.; Xiao, Z.; Zhang, H.; Li, Z.; Zhuang, J.; Peng, C.; Huang, Y. Negligible hysteresis planar perovskite solar cells using Ga-doped SnO₂ nanocrystal as electron transport layers. *Org. Electron.* **2019**, *71*, 98–105. [[CrossRef](#)]
9. Ball, J.M.; Lee, M.M.; Hey, A.; Snaith, H.J. Low-temperature processed meso-superstructured to thin-film perovskite solar cells. *Energy Environ. Sci.* **2013**, *6*, 1739–1743. [[CrossRef](#)]
10. Liu, Z.; Chang, J.; Lin, Z.; Zhou, L.; Yang, Z.; Chen, D.; Zhang, C.; Liu, S.; Hao, Y. High-Performance Planar Perovskite Solar Cells Using Low Temperature, Solution-Combustion-Based Nickel Oxide Hole Transporting Layer with Efficiency Exceeding 20%. *Adv. Energy Mater.* **2018**, *8*, 1703432. [[CrossRef](#)]
11. You, J.; Meng, L.; Song, T.-B.; Guo, T.-F.; Yang, Y.M.; Chang, W.-H.; Hong, Z.; Chen, H.; Zhou, H.; Chen, Q. Improved air stability of perovskite solar cells via solution-processed metal oxide transport layers. *Nat. Nanotechnol.* **2016**, *11*, 75–81. [[CrossRef](#)]
12. Zhao, D.; Sexton, M.; Park, H.; Baure, G.; Nino, J.C.; So, F. High-efficiency solution-processed planar perovskite solar cells with a polymer hole transport layer. *Adv. Energy Mater.* **2015**, *5*, 1401855. [[CrossRef](#)]
13. Lai, W.; Lin, K.; Wang, Y.; Chiang, T.; Chen, P.; Guo, T. Oxidized Ni/Au transparent electrode in efficient CH₃NH₃PbI₃ perovskite/fullerene planar heterojunction hybrid solar cells. *Adv. Mater.* **2016**, *28*, 3290–3297. [[CrossRef](#)] [[PubMed](#)]
14. Yin, X.; Chen, P.; Que, M.; Xing, Y.; Que, W.; Niu, C.; Shao, J. Highly efficient flexible perovskite solar cells using solution-derived NiOx hole contacts. *ACS Nano* **2016**, *10*, 3630–3636. [[CrossRef](#)] [[PubMed](#)]
15. Seo, S.; Park, I.J.; Kim, M.; Lee, S.; Bae, C.; Jung, H.S.; Park, N.-G.; Kim, J.Y.; Shin, H. An ultra-thin, un-doped NiO hole transporting layer of highly efficient (16.4%) organic-inorganic hybrid perovskite solar cells. *Nanoscale* **2016**, *8*, 11403–11412. [[CrossRef](#)] [[PubMed](#)]
16. Kim, J.; Lee, H.R.; Kim, H.P.; Lin, T.; Kanwat, A.; bin Mohd Yusoff, A.R.; Jang, J. Effects of UV-ozone irradiation on copper doped nickel acetate and its applicability to perovskite solar cells. *Nanoscale* **2016**, *8*, 9284–9292. [[CrossRef](#)]
17. Yin, X.; Yao, Z.; Luo, Q.; Dai, X.; Zhou, Y.; Zhang, Y.; Zhou, Y.; Luo, S.; Li, J.; Wang, N. High efficiency inverted planar perovskite solar cells with solution-processed NiOx hole contact. *ACS Appl. Mater. Interfaces* **2017**, *9*, 2439–2448. [[CrossRef](#)]
18. Shibayama, N.; Kanda, H.; Yusa, S.; Fukumoto, S.; Baranwal, A.K.; Segawa, H.; Miyasaka, T.; Ito, S. All-inorganic inverse perovskite solar cells using zinc oxide nanocolloids on spin coated perovskite layer. *Nano Converg.* **2017**, *4*, 18. [[CrossRef](#)]
19. Park, J.H.; Seo, J.; Park, S.; Shin, S.S.; Kim, Y.C.; Jeon, N.J.; Shin, H.; Ahn, T.K.; Noh, J.H.; Yoon, S.C. Efficient CH₃NH₃PbI₃ perovskite solar cells employing nanostructured p-type NiO electrode formed by a pulsed laser deposition. *Adv. Mater.* **2015**, *27*, 4013–4019. [[CrossRef](#)]
20. Corani, A.; Li, M.-H.; Shen, P.-S.; Chen, P.; Guo, T.-F.; El Nahhas, A.; Zheng, K.; Yartsev, A.; Sundström, V.; Ponseca, C.S., Jr. Ultrafast dynamics of hole injection and recombination in organometal halide perovskite using nickel oxide as p-type contact electrode. *J. Phys. Chem. Lett.* **2016**, *7*, 1096–1101. [[CrossRef](#)]
21. Chen, W.; Wu, Y.; Liu, J.; Qin, C.; Yang, X.; Islam, A.; Cheng, Y.-B.; Han, L. Hybrid interfacial layer leads to solid performance improvement of inverted perovskite solar cells. *Energy Environ. Sci.* **2015**, *8*, 629–640. [[CrossRef](#)]
22. Kim, J.H.; Liang, P.; Williams, S.T.; Cho, N.; Chueh, C.; Glaz, M.S.; Ginger, D.S.; Jen, A.K. High-performance and environmentally stable planar heterojunction perovskite solar cells based on a solution-processed copper-doped nickel oxide hole-transporting layer. *Adv. Mater.* **2015**, *27*, 695–701. [[CrossRef](#)] [[PubMed](#)]
23. Kaneko, R.; Chowdhury, T.H.; Wu, G.; Kayesh, M.E.; Kazaoui, S.; Sugawa, K.; Lee, J.-J.; Noda, T.; Islam, A.; Otsuki, J. Cobalt-doped nickel oxide nanoparticles as efficient hole transport materials for low-temperature processed perovskite solar cells. *Sol. Energy* **2019**, *181*, 243–250. [[CrossRef](#)]
24. Nie, W.; Tsai, H.; Blancon, J.; Liu, F.; Stoumpos, C.C.; Traore, B.; Kepenekian, M.; Durand, O.; Katan, C.; Tretiak, S. Critical role of interface and crystallinity on the performance and photostability of perovskite solar cell on nickel oxide. *Adv. Mater.* **2018**, *30*, 1703879. [[CrossRef](#)] [[PubMed](#)]
25. Ren, G.; Li, Z.; Wu, W.; Han, S.; Liu, C.; Li, Z.; Dong, M.; Guo, W. Performance improvement of planar perovskite solar cells with cobalt-doped interface layer. *Appl. Surf. Sci.* **2020**, *507*, 145081. [[CrossRef](#)]

26. Sidhik, S.; Cerdan Pasaran, A.; Esparza, D.; Lopez Luke, T.; Carriles, R.; De la Rosa, E. Improving the optoelectronic properties of mesoporous TiO₂ by cobalt doping for high-performance hysteresis-free perovskite solar cells. *ACS Appl. Mater. Interfaces* **2018**, *10*, 3571–3580. [[CrossRef](#)]
27. Ren, X.; Xie, L.; Kim, W.B.; Lee, D.G.; Jung, H.S.; Liu, S. Chemical Bath Deposition of Co-Doped TiO₂ Electron Transport Layer for Hysteresis-Suppressed High-Efficiency Planar Perovskite Solar Cells. *Sol. RRL* **2019**, *3*, 1900176. [[CrossRef](#)]
28. Shannon, R.D. Crystal physics, diffraction, theoretical and general crystallography. *Acta Cryst. A* **1976**, *32*, 751–767. [[CrossRef](#)]
29. Xie, Y.; Lu, K.; Duan, J.; Jiang, Y.; Hu, L.; Liu, T.; Zhou, Y.; Hu, B. Enhancing Photovoltaic Performance of Inverted Planar Perovskite Solar Cells by Cobalt-Doped Nickel Oxide Hole Transport Layer. *ACS Appl. Mater. Interfaces* **2018**, *10*, 14153–14159. [[CrossRef](#)]
30. Lee, P.-H.; Li, B.-T.; Lee, C.-F.; Huang, Z.-H.; Huang, Y.-C.; Su, W.-F. High-efficiency perovskite solar cell using cobalt doped nickel oxide hole transport layer fabricated by NIR process. *Sol. Energy Mater. Sol. Cells* **2020**, *208*, 110352. [[CrossRef](#)]
31. Kim, S.; Jeong, J.-E.; Hong, J.; Lee, K.; Lee, M.J.; Woo, H.Y.; Hwang, I. Improved Interfacial Crystallization by Synergic Effects of Precursor Solution Stoichiometry and Conjugated Polyelectrolyte Interlayer for High Open-Circuit Voltage of Perovskite Photovoltaic Diodes. *ACS Appl. Mater. Interfaces* **2020**, *12*, 12328–12336. [[CrossRef](#)]
32. Rawat, S.S.; Kumar, A.; Srivastava, R.; Suman, C.K. Efficiency Enhancement in Organic Solar Cells by Use of Cobalt Phthalocyanine (CoPc) Thin Films. *J. Nanosci. Nanotechnol.* **2020**, *20*, 3703–3709. [[CrossRef](#)] [[PubMed](#)]
33. Wang, G.; Wang, L.; Qiu, J.; Yan, Z.; Li, C.; Dai, C.; Zhen, C.; Tai, K.; Yu, W.; Jiang, X. In Situ Passivation on Rear Perovskite Interface for Efficient and Stable Perovskite Solar Cells. *ACS Appl. Mater. Interfaces* **2020**, *12*, 7690–7700. [[CrossRef](#)]
34. Nie, W.; Tsai, H.; Asadpour, R.; Blancon, J.-C.; Neukirch, A.J.; Gupta, G.; Crochet, J.J.; Chhowalla, M.; Tretiak, S.; Alam, M.A. High-efficiency solution-processed perovskite solar cells with millimeter-scale grains. *Science* **2015**, *347*, 522–525. [[CrossRef](#)]
35. Jiang, F.; Choy, W.C.H.; Li, X.; Zhang, D.; Cheng, J.; Non, P.-F.S.-P. stoichiometric NiOx Nanoparticles for Efficient Hole-Transport Layers of Organic Optoelectronic Devices. *Adv. Mater.* **2015**, *27*, 2930–2937. [[CrossRef](#)]
36. Méndez, P.F.; Muhammed, S.K.M.; Barea, E.M.; Masi, S.; Mora-Seró, I. Analysis of the UV–Ozone-Treated SnO₂ Electron Transporting Layer in Planar Perovskite Solar Cells for High Performance and Reduced Hysteresis. *Sol. RRL* **2019**, *3*, 1900191. [[CrossRef](#)]
37. Saliba, M.; Correa-Baena, J.-P.; Wolff, C.M.; Stolterfoht, M.; Phung, N.; Albrecht, S.; Neher, D.; Abate, A. How to Make over 20% Efficient Perovskite Solar Cells in Regular (n–i–p) and Inverted (p–i–n) Architectures. *Chem. Mater.* **2018**, *30*, 4193–4201. [[CrossRef](#)]
38. Fominykh, K.; Tok, G.C.; Zeller, P.; Hajiyani, H.; Miller, T.; Döblinger, M.; Pentcheva, R.; Bein, T.; Fattakhova-Rohlfing, D. Rock Salt Ni/Co Oxides with Unusual Nanoscale-Stabilized Composition as Water Splitting Electrocatalysts. *Adv. Funct. Mater.* **2017**, *27*, 1605121. [[CrossRef](#)]
39. He, Q.; Yao, K.; Wang, X.; Xia, X.; Leng, S.; Li, F. Room-temperature and solution-processable Cu-doped nickel oxide nanoparticles for efficient hole-transport layers of flexible large-area perovskite solar cells. *ACS Appl. Mater. Interfaces* **2017**, *9*, 41887–41897. [[CrossRef](#)] [[PubMed](#)]
40. Natu, G.; Hasin, P.; Huang, Z.; Ji, Z.; He, M.; Wu, Y. Valence band-edge engineering of nickel oxide nanoparticles via cobalt doping for application in p-type dye-sensitized solar cells. *ACS Appl. Mater. Interfaces* **2012**, *4*, 5922–5929. [[CrossRef](#)] [[PubMed](#)]
41. Lee, J.H.; Noh, Y.W.; Jin, I.S.; Park, S.H.; Jung, J.W. A solution-processed cobalt-doped nickel oxide for high efficiency inverted type perovskite solar cells. *J. Power Sources* **2019**, *412*, 425–432. [[CrossRef](#)]
42. Zhang, J.; Wang, J.; Fu, Y.; Zhang, B.; Xie, Z. Efficient and stable polymer solar cells with annealing-free solution-processible NiO nanoparticles as anode buffer layers. *J. Mater. Chem. C* **2014**, *2*, 8295–8302. [[CrossRef](#)]
43. Chen, W.; Liu, F.; Feng, X.; Djurišić, A.B.; Chan, W.K.; He, Z. Cesium doped NiOx as an efficient hole extraction layer for inverted planar perovskite solar cells. *Adv. Energy Mater.* **2017**, *7*, 1700722. [[CrossRef](#)]

44. Stolterfoht, M.; Le Corre, V.M.; Feuerstein, M.; Caprioglio, P.; Koster, L.J.A.; Neher, D. Voltage-Dependent Photoluminescence and How It Correlates with the Fill Factor and Open-Circuit Voltage in Perovskite Solar Cells. *ACS Energy Lett.* **2019**, *4*, 2887–2892. [[CrossRef](#)]
45. Contreras-Bernal, L.; Ramos-Terrón, S.; Riquelme, A.; Boix, P.P.; Idígoras, J.; Mora-Seró, I.; Anta, J.A. Impedance analysis of perovskite solar cells: A case study. *J. Mater. Chem. A* **2019**, *7*, 12191–12200. [[CrossRef](#)]
46. Tress, W.; Yavari, M.; Domanski, K.; Yadav, P.; Niesen, B.; Baena, J.P.C.; Hagfeldt, A.; Graetzel, M. Interpretation and evolution of open-circuit voltage, recombination, ideality factor and subgap defect states during reversible light-soaking and irreversible degradation of perovskite solar cells. *Energy Environ. Sci.* **2018**, *11*, 151–165. [[CrossRef](#)]



© 2020 by the authors. Licensee MDPI, Basel, Switzerland. This article is an open access article distributed under the terms and conditions of the Creative Commons Attribution (CC BY) license (<http://creativecommons.org/licenses/by/4.0/>).